



Deposited via The University of Sheffield.

White Rose Research Online URL for this paper:

<https://eprints.whiterose.ac.uk/id/eprint/96196/>

Version: Accepted Version

Article:

Singh, N., Verhoosel, C.V., de Borst, R. et al. (2016) A fracture-controlled path-following technique for phase-field modeling of brittle fracture. *Finite Elements in Analysis and Design*, 113. pp. 14-29. ISSN: 0168-874X

<https://doi.org/10.1016/j.finel.2015.12.005>

Article available under the terms of the CC-BY-NC-ND licence
(<https://creativecommons.org/licenses/by-nc-nd/4.0/>)

Reuse

Items deposited in White Rose Research Online are protected by copyright, with all rights reserved unless indicated otherwise. They may be downloaded and/or printed for private study, or other acts as permitted by national copyright laws. The publisher or other rights holders may allow further reproduction and re-use of the full text version. This is indicated by the licence information on the White Rose Research Online record for the item.

Takedown

If you consider content in White Rose Research Online to be in breach of UK law, please notify us by emailing eprints@whiterose.ac.uk including the URL of the record and the reason for the withdrawal request.

A fracture-controlled path-following technique for phase-field modeling of brittle fracture

N. Singh^a, C.V. Verhoosel^{a,*}, R. de Borst^b, E. H. van Brummelen^a

^a*Department of Mechanical Engineering, Eindhoven University of Technology, 5600 MB Eindhoven, The Netherlands*

^b*School of Engineering, University of Glasgow, Glasgow G12 8LT, UK*

Abstract

In the phase-field description of brittle fracture, the fracture-surface area can be expressed as a functional of the phase field (or damage field). In this work we study the applicability of this explicit expression as a (non-linear) path-following constraint to robustly track the equilibrium path in quasi-static fracture propagation simulations, which can include snap-back phenomena. Moreover, we derive a fracture-controlled staggered solution procedure by systematic decoupling of the path-following controlled elasticity and phase-field problems. The fracture-controlled monolithic and staggered solution procedures are studied for a series of numerical test cases. The numerical results demonstrate the robustness of the new approach, and provide insight in the advantages and disadvantages of the monolithic and staggered procedures.

Keywords: Brittle fracture, Phase-field modeling, Path-following methods, Staggered solution procedures

1. Introduction

2 In many problems in brittle-fracture mechanics, phenomena such as nu-
3 cleation, propagation, branching and merging occur. Complex crack patterns
4 appear as a consequence of *e.g.* the presence of multiple cracks, anisotropy

*Corresponding author. Phone: +31 40 247 2382

Email addresses: n.singh@tue.nl (N. Singh), c.v.verhoosel@tue.nl
(C.V. Verhoosel), rene.deborst@glasgow.ac.uk (R. de Borst),
e.h.v.brummelen@tue.nl (E. H. van Brummelen)

5 and heterogeneity. Using discrete fracture models it is generally difficult to
6 capture such topologically complex crack patterns, which has led to the devel-
7 opment of smeared or continuum crack models, including phase-field models
8 [1, 2]. In phase-field models the crack surface is regularized by a smeared
9 damage (or phase-field) function, which avoids the need for the explicit track-
10 ing of fracture surfaces. Over the past years phase-field modeling of fracture
11 has been applied to a wide range of problems, including dynamic fractur-
12 ing [3, 4], large deformation fracturing [5], fracturing of electromechanical
13 materials [6], cohesive fracturing [7], and fluid-driven fracture propagation
14 [8].

15 In this work we consider the quasi-static evolution of brittle fractures in
16 an elastic solid, where fractures are driven by gradual incrementation of the
17 loading conditions. Since softening and snap-back behavior are frequently en-
18 countered in such situations, path-following control is required to adequately
19 track the complete equilibrium path [9]. Path-following techniques have been
20 an indispensable tool in non-linear solid mechanics since the pioneering works
21 of Riks [10], Crisfield [11] and Ramm [12]. While these path-following tech-
22 niques were developed in the context of snap-back behavior caused by geo-
23 metrical non-linearities, over the past decades various enhancements to the
24 original path-following procedures have been proposed in order to increase
25 their versatility and computational efficiency.

26 A particularly interesting application of path-following techniques is their
27 use to track snap-back behavior as a result of material non-linearities, es-
28 pecially localized failure phenomena. In such situations the original path-
29 following constraints have proven to lack robustness by the fact that they
30 fail to account for the localized nature of the source of non-linearity. Various
31 modified techniques have been proposed to account for this localized behav-
32 ior, among which are a series of (semi-)automatic procedures for selecting
33 degrees of freedom that contribute to the nonlinear behavior of the system
34 [13, 14]. Our work builds on the idea that an appropriate path-following
35 technique can be obtained by selecting a physically-motivated constraint
36 equation. In this regard the crack mouth opening displacement (CMOD)
37 and crack mouth sliding displacement (CMSD) control equations proposed
38 by De Borst [15] can be considered as pioneering works. Inspired by these
39 control equations energy-release rate path-following control was developed
40 for the simulation of localized failure phenomena, including discrete crack-
41 ing, smeared damage and softening plasticity [16, 17]. The versatility of the
42 energy-release rate control has been demonstrated for a variety of applica-

43 tions, including cases in which geometrical and material nonlinearities are
44 competing [18].

45 When applied in the context of discrete fracture simulations, the energy
46 release-rate path-following technique has the ability to indirectly control the
47 rate at which a fracture propagates by proper selection of the energy dissi-
48 pation increment. In Ref. [19] it has been shown that the energy-release rate
49 control can be successfully applied to phase-field simulations, where the dis-
50 sipation increment is related to the fracture-surface area increment through
51 the critical energy release rate. In the case of phase-field simulations the
52 relation between the path-following constraint and the fracture-surface area
53 increase can be made explicit, *i.e.* the fracture-surface area can be expressed
54 as a functional of the phase-field solution. This allows for direct prescription
55 of the surface-area increments. This explicit dependence allows for the se-
56 lection of the path-following parameter increment based on a criterion that
57 relates the crack surface growth to the size of the employed (finite element)
58 mesh, which provides a natural way of controlling the accuracy of the path-
59 following scheme. In this work we formulate and study such a fracture-based
60 path-following technique, which – if used in combination with a monolithic
61 incremental-iterative path-following procedure – allows for the parametriza-
62 tion of the equilibrium path by specified fracture-surface area increments.

63 Quasi-static phase-field simulations of brittle fracture phenomena have
64 mostly relied on the use of a staggered solution strategy, in which the elas-
65 ticity problem and phase-field problems are decoupled [2]. This staggered
66 solution strategy has been proven to be computationally efficient. A draw-
67 back of this solution strategy is that the step sizes need to be selected ap-
68 propriately in order to control the accuracy of the procedure. The currently
69 available staggered schemes are not capable of representing snap-back behav-
70 ior. In this work a staggered fracture-based path-following method is derived
71 from the monolithic scheme, which has the possibility of reducing the com-
72 putational effort of the monolithic scheme at the cost of only satisfying the
73 path-following increments in an approximate sense. This fracture-controlled
74 staggered scheme does, however, inherit the property of the underlying mono-
75 lithic scheme that the fracture propagation increments can directly be con-
76 trolled (albeit in an approximate sense). This simplifies the selection of the
77 step size compared to *e.g.* the displacement-based staggered scheme.

78 In Section 2 we introduce the phase-field formulation for brittle fracture
79 and its discretization using the finite element method. In Section 3 we derive
80 the fracture-based path-following constraint. In this section we also discuss

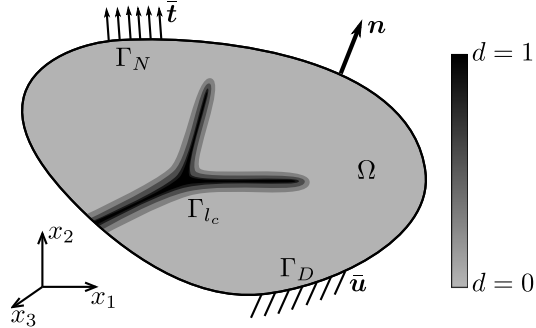


Figure 1: Schematic representation of a domain Ω with regularized fracture surface $\Gamma_{l_c}(d)$ representing a fractured solid medium.

81 various aspects of the corresponding incremental-iterative path-following pro-
 82 cedure. In Section 4 we systematically derive the staggered path-following
 83 scheme, after which the monolithic scheme and staggered scheme are studied
 84 in detail in terms of computational effort and accuracy in Section 5. In this
 85 section we also study the nature of the snap-back behavior encountered in
 86 phase-field simulations for brittle fracture. Finally, conclusions are drawn in
 87 Section 6.

88 2. Phase-field formulation for brittle fracture

89 2.1. Problem formulation

90 We consider the evolution of a regularized fracture surface, $\Gamma_{l_c}(d)$, in an
 91 n_{dim} -dimensional elastic medium, $\Omega \subset \mathbb{R}^{n_{\text{dim}}}$, under quasi-static loading (see
 92 Figure 1). The outward-pointing unit normal vector to the surface of the
 93 domain Ω is denoted by $\mathbf{n} : \Gamma \rightarrow \mathbb{R}^{n_{\text{dim}}}$. Small deformations and deformation
 94 gradients are assumed, and the deformation of the medium is described by the
 95 displacement field $\mathbf{u} : \Omega \rightarrow \mathbb{R}^{n_{\text{dim}}}$. The fracture surface, $\Gamma_{l_c}(d)$, is represented
 96 by the phase field $d : \Omega \rightarrow [0, 1]$, which approaches 1 inside a regularized
 97 crack and vanishes far away from the fracture surface. External tractions, $\bar{\mathbf{t}}$,
 98 are applied along the Neumann boundary Γ_N and prescribed displacements,
 99 $\bar{\mathbf{u}}$, are considered at the Dirichlet boundary Γ_D .

Under the above conditions, the strong form for the displacement and

phase field is given by:

$$(S) \quad \begin{cases} \nabla \cdot \boldsymbol{\sigma} = \mathbf{0} & \text{in } \Omega & (1a) \\ \frac{\mathcal{G}_c}{l_c} (d - l_c^2 \Delta d) = 2(1 - d)\mathcal{H} & \text{in } \Omega & (1b) \\ \boldsymbol{\sigma} \cdot \mathbf{n} = \bar{\mathbf{t}} & \text{on } \Gamma_N & (1c) \\ \mathbf{u} = \bar{\mathbf{u}} & \text{on } \Gamma_D & (1d) \\ \nabla d \cdot \mathbf{n} = 0 & \text{on } \Gamma & (1e) \end{cases}$$

100 In this strong form, \mathcal{G}_c is the Griffith type critical energy-release rate and l_c is
 101 the length scale associated with the phase-field regularization of the fracture
 102 surface¹ (*i.e.* the width of the cracks) [1, 2]. In order to restrict the fracturing
 103 process to tensile stress states, the Cauchy stress tensor in the above problem
 104 is defined as

$$\boldsymbol{\sigma}(\boldsymbol{\varepsilon}, d) = g(d)\boldsymbol{\sigma}_0^+(\boldsymbol{\varepsilon}) + \boldsymbol{\sigma}_0^-(\boldsymbol{\varepsilon}), \quad (2)$$

105 where $g(d) = (1 - d)^2$ is the degradation function, $\boldsymbol{\sigma}_0^+$ and $\boldsymbol{\sigma}_0^-$ are the tensile
 106 and compressive parts of the virgin ($d = 0$) Cauchy stress tensor [2], and
 107 $\boldsymbol{\varepsilon} = \nabla^s \mathbf{u}$ is the infinitesimal strain tensor. From the above stress definition it
 108 evidently follows that this degradation function must satisfy the conditions
 109 $g(0) = 1$ and $g(1) = 0$. The property that $g'(1) = 0$ ensures that the
 110 thermodynamic driving force for the phase-field model (*i.e.* the right-hand-
 111 side of the phase-field equation) vanishes once a fracture has completely
 112 evolved.

Irreversibility, *i.e.* the notion that the fracture surface can only extend
 ($\dot{\Gamma}_{l_c} \geq 0$), is enforced in the strong form (1) by means of the history field
 $\mathcal{H} : \Omega \rightarrow \mathbb{R}^+$. This history field satisfies the Kuhn-Tucker conditions for
 loading and unloading, defined as

$$\psi_0^+ - \mathcal{H} \leq 0, \quad \dot{\mathcal{H}} \geq 0, \quad \dot{\mathcal{H}}(\psi_0^+ - \mathcal{H}) = 0, \quad (3)$$

113 with ψ_0^+ the tensile part of the virgin elastic energy density.

114 2.2. Finite element discretization

To compute an approximate solution to the strong form (1) using the
 finite element method, the weak form is derived. Using the function spaces

¹Here the length scale l_c is defined as in Ref. [2]. We note that in literature sometimes
 use is made of the alternative length scale definition $\varepsilon = l_c/2$, *e.g.* [1].

$\mathcal{V}^u = \{\mathbf{u} \in \mathbf{H}^1(\Omega) \mid \mathbf{u} = \bar{\mathbf{u}} \text{ on } \Gamma_D\}$ and $\mathcal{V}^d = H^1(\Omega)$ for the trial functions, and $\mathcal{V}_0^u = \{\mathbf{u} \in \mathbf{H}^1(\Omega) \mid \mathbf{u} = \mathbf{0} \text{ on } \Gamma_D\}$ and \mathcal{V}^d for the test functions, we obtain:

$$(W) \begin{cases} \text{Find } (\mathbf{u}, d) \in \mathcal{V}^u \times \mathcal{V}^d \text{ such that:} \\ \int_{\Omega} \boldsymbol{\sigma} : \nabla^s \mathbf{w} dV = \int_{\Gamma_N} \bar{\mathbf{t}} \cdot \mathbf{w} dS & \forall \mathbf{w} \in \mathcal{V}_0^u \quad (4a) \\ \int_{\Omega} \left[\left(\frac{\mathcal{G}_c}{l_c} + 2\mathcal{H} \right) d - 2\mathcal{H} \right] e + \mathcal{G}_c l_c \nabla d \cdot \nabla e dV = 0 & \forall e \in \mathcal{V}^d \quad (4b) \end{cases}$$

This weak form is discretized using a (Bubnov-) Galerkin finite element discretization, for which the displacement field and phase field are interpolated by

$$\mathbf{u}(\mathbf{x}) = \sum_{I=1}^{n^u} \mathbf{N}_I^u(\mathbf{x}) a_I^u, \quad d(\mathbf{x}) = \sum_{I=1}^{n^d} N_I^d(\mathbf{x}) a_I^d, \quad (5)$$

115 where n^u and n^d denote the number of displacement and phase field degrees of
 116 freedom, respectively. The vector-valued shape functions $\mathbf{N}_I^u(\mathbf{x}) : \Omega \rightarrow \mathbb{R}^{n^{\text{dim}}}$
 117 and scalar-valued shape functions $N_I^d : \Omega \rightarrow \mathbb{R}$ span subsets of $\mathbf{H}^1(\Omega)$ and
 118 $H^1(\Omega)$, respectively. The nodal displacement components and phase-field
 119 values are respectively represented by $\mathbf{a}^u \in \mathbb{R}^{n^u}$ and $\mathbf{a}^d \in \mathbb{R}^{n^d}$. The degrees of
 120 freedom are assembled in a single vector of coefficients: $\mathbf{a}^T = [\mathbf{a}^{u^T}, \mathbf{a}^{d^T}]$. The
 121 Dirichlet boundary conditions are enforced strongly by means of a constraints
 122 matrix \mathbf{C} , such that $\mathbf{a} = \mathbf{C}\mathbf{a}_f + \mathbf{a}_p$, with \mathbf{a}_f the free degrees of freedom and
 123 \mathbf{a}_p the prescribed degrees of freedom.

124 Using the finite element discretization (5), the weak form (4) can be
 125 written as a non-linear system of equations

$$\mathbf{f}_{\text{int}}(\mathbf{a}) = \mathbf{f}_{\text{ext}}, \quad (6)$$

126 with $\mathbf{f}_{\text{int}}^T = [\mathbf{f}_{\text{int}}^{u^T}, \mathbf{f}_{\text{int}}^{d^T}]$ and $\mathbf{f}_{\text{ext}}^T = [\mathbf{f}_{\text{ext}}^{u^T}, \mathbf{0}^T]$, see Appendix A for the expres-
 127 sions of these force vectors.

128 3. Fracture-controlled monolithic solution procedure

129 Commonly, the solution to the quasi-static nonlinear problem (6) is com-
 130 puted through an incremental-iterative solution procedure. In such a pro-
 131 cedure either the external loading ($\mathbf{f}_{\text{ext}}^k$) or the boundary displacement (\mathbf{a}_p^k)

132 is prescribed in a stepwise incremental fashion, with index $k = 1, \dots, n_{\text{steps}}$.
 133 In every step, the corresponding solution increment, $\Delta \mathbf{a}^k = \mathbf{a}^k - \mathbf{a}^{k-1}$, is
 134 computed using Newton-Raphson iterations. The tangent stiffness matrices
 135 required by the Newton solution procedure can be found in Appendix A.

136 Evidently, force-controlled and displacement-controlled solution proce-
 137 dures break down in the case of softening or snap-back behavior, respectively;
 138 see *e.g.* [9]. Therefore, in order to track the complete equilibrium path we
 139 need to supplement the system of equations with a path-following control.

140 In this contribution we restrict ourselves to the case of proportional load-
 141 ing, *i.e.* we assume that the external force vector $\mathbf{f}_{\text{ext}}^k$ can be written as
 142 a load level λ^k times a “unit” load vector $\hat{\mathbf{f}}$ in the case of force loading,
 143 and the boundary displacements are expressed as $\mathbf{a}_p^k = \lambda^k \hat{\mathbf{a}}$ in the case of
 144 displacement loading.

145 The monolithic path-following procedure is outlined in the pseudo-code
 146 Algorithm 1. This standard algorithm is here presented to place some specific
 147 algorithmic aspects of the current work in the proper perspective (see Section
 148 3.3). Moreover, this algorithm will serve as the basis for the novel staggered
 149 path-following procedure to be derived in the next section.

150 3.1. The path-following constraint

151 Using a path-following technique, the equilibrium path is defined as the
 152 set of all points $\{(\mathbf{a}(t), \lambda(t)) | t \in [0, T]\}$ which are a solution to the non-linear
 153 system of equations (6), where t represents the time parameter ranging
 154 from 0 to the final time T . In practice the equilibrium path is represented
 155 by a finite sequence of equilibrium points $\{(\mathbf{a}^k, \lambda^k)\}_{k=0}^{n_{\text{steps}}}$, computed through
 156 the above-mentioned incremental-iterative solution procedure. In order to
 157 compute the discrete equilibrium points, the general idea of path-following
 158 techniques is to supplement the system of equations (6) with a path-following
 159 constraint of the form

$$\zeta(\mathbf{a}^k, \Delta \mathbf{a}^k, \lambda^k, \Delta \lambda^k; \Delta \tau) = 0, \quad (7)$$

160 where $\Delta \tau > 0$ is the positive increment of the path-following parameter τ ,
 161 which can be regarded as a pseudo-time parameter. By the incremental-
 162 iterative solution of the non-linear system of equations (6) in combination
 163 with this constraint equation, a discrete parametrization of the equilibrium
 164 path in terms of the path-following parameter τ is obtained: $\{\mathbf{a}(\tau^k), \lambda(\tau^k)\}_{k=0}^{n_{\text{steps}}}$.
 165 We note that the case of force control, *i.e.* $\lambda^k = \lambda^{k-1} + \dot{\lambda} \Delta \tau$, is in fact the

```

Input:  $(\mathbf{a}^0, \lambda^0), \mathcal{H}^0$  #State vector, load level & history field
Output:  $(\mathbf{a}^1, \lambda^1), (\mathbf{a}^2, \lambda^2), \dots, (\mathbf{a}^{n_{\text{steps}}}, \lambda^{n_{\text{steps}}})$  #Discrete eq. path

#Initialization
control = 'displacement'

#Load steps
for  $k = 1, \dots, n_{\text{steps}}$  :
     $\mathbf{a}_0^k = \mathbf{a}^{k-1}, \lambda_0^k = \lambda^{k-1}$  #Initialization of Newton iterations

    #Newton iterations
    for  $m = 1, \dots, m_{\text{max}}$  :
         $\mathbf{f}_{\text{int}}, \mathbf{K} = \text{assemble\_augmented\_system}(\mathbf{a}_{m-1}^k, \lambda_{m-1}^k, \mathcal{H}^{k-1})$ 
         $\zeta, \mathbf{h}, q = \text{assemble\_control\_equation}(\mathbf{a}_{m-1}^k, \lambda_{m-1}^k, \text{control})$ 
         $\mathbf{a}_m^k, \lambda_m^k = \text{solve\_augmented\_system}(\mathbf{K}, \mathbf{f}_{\text{int}}, \zeta, \mathbf{h}, q)$ 
        converged = check_convergence( $\mathbf{a}_m^k, \lambda_m^k$ )
        if converged : break
    end

    if converged :
         $\mathbf{a}^k = \mathbf{a}_m^k, \lambda^k = \lambda_m^k$  #Update state vector and load level
         $\mathcal{H}^k = \text{update\_history\_field}(\mathbf{a}^k, \mathcal{H}^{k-1})$ 
        control = select_control_equation( $\mathbf{a}^k, \mathcal{H}^k$ )
    else:
        restart_newton_iterations()
    end
end
end

```

Algorithm 1: Monolithic incremental-iterative path-following procedure

166 most simple case of path-following control possible: $\zeta = \Delta\lambda^k - \dot{\lambda}\Delta\tau = 0$,
 167 where $\dot{\lambda}$ represents a prescribed loading rate.

168 The choice for a particular path-following constraint is dictated by the
 169 existence of solutions to the non-linear system of equations (6) upon the
 170 incrementation of the path parameter τ . For example, force control will
 171 be unable to represent softening behavior, while displacement control will
 172 fail when snap-back occurs. In fracture mechanics problems various path-
 173 following constraints have been found to be very effective. The CMOD (or
 174 CMSD) control proposed in [15] has successfully been applied in many cases.
 175 Over the past decade the use of dissipation-based control has been studied
 176 extensively and was found to be very reliable for problems in which severe
 177 non-linear behavior is expected [17]. The rationale behind the dissipation-
 178 based control is that, from a physical perspective, dissipation has to be non-
 179 negative as a consequence of the irreversibility of fracture propagation. When
 180 fracture propagation is the dominant source of dissipation, this control is very
 181 effective in simulating the evolution of fractures.

182 Inspired by the idea of dissipation-control, in this contribution we pro-
 183 pose a path-following constraint directly based on the fracture-surface area
 184 (or fracture length in 2D). This has become tractable only with the intro-
 185 duction of phase-field models for brittle fracture, due to the availability of
 186 an explicit functional expression for the fracture-surface area. We note that
 187 in the case of Griffith's theory of fracture, there is a direct relation between
 188 the fracture-surface area and the amount of dissipation, and hence, under
 189 specific assumptions, the control equation developed herein is identical to
 190 that developed in [16] (see Appendix B for details).

191 *3.2. Fracture-based path-following constraint*

192 In the phase-field formulation for brittle fracture, the fracture surface
 193 area is expressed by

$$\Gamma_{l_c}(d) = \frac{1}{2l_c} \int_{\Omega} d^2 + l_c^2 |\nabla d|^2 \, dV. \quad (8)$$

194 In this work we prescribe the rate of fracture propagation, $\dot{\Gamma}_{l_c}$, by means of
 195 the path-following constraint

$$\begin{aligned} \zeta &= \Gamma_{l_c}(d^k) - \dot{\Gamma}_{l_c} \tau^k \\ &= \Gamma_{l_c}(d^k) - \Gamma_{l_c}(d^{k-1}) - \dot{\Gamma}_{l_c} \Delta\tau \end{aligned} \quad (9)$$

Note that this path-following constraint is a non-linear equation of the phase field. Since we apply this constraint in a Newton-Raphson solution procedure, it is required to compute the derivative of this constraint with respect to the nodal displacements, and nodal phase-field coefficients, which yields:

$$\mathbf{h}^u = \frac{\partial \zeta}{\partial \mathbf{a}^u} = \mathbf{0} \quad \mathbf{h}^d = \frac{\partial \zeta}{\partial \mathbf{a}^d} = \frac{1}{l_c} \int_{\Omega} d \mathbf{N}^d + l_c^2 \nabla d \cdot \nabla \mathbf{N}^d dV \quad (10)$$

196 with \mathbf{N}^d the column vector of phase-field shape functions. In the remainder
 197 we will consider the combined vector $\mathbf{h}^T = [\mathbf{h}^{u^T}, \mathbf{h}^{d^T}]$. Since the constraint
 198 (9) does not depend on the load level explicitly, it follows that

$$q = \frac{\partial \zeta}{\partial \lambda} = 0. \quad (11)$$

199 The fracture-based path-following constraint (9) has two major benefits.
 200 First, it is evident that the path-following parameter is non-decreasing in
 201 time, and hence this constraint choice is anticipated to yield robust results,
 202 also in the case of material softening and/or snapback. The second advantage
 203 is that this choice for the constraint provides an intuitive way of selecting
 204 the appropriate step size. By requiring that the fracture surface should not
 205 propagate across multiple elements within in a single step, the irreversibility
 206 condition can be adequately imposed. We will further study the choice of
 207 the step size in Section 5.

208 3.3. Algorithmic aspects

209 In this section we discuss three algorithmic aspects that are specific to the
 210 current work: *i*) the solution of the augmented system of equations within
 211 each Newton-Raphson iteration; *ii*) the convergence criterion employed for
 212 the phase-field model; and *iii*) the initialization and selection procedure for
 213 the control equation and the restarting procedure for the Newton-Raphson
 214 iterations.

215 3.3.1. Solving the augmented system of equations

216 The solution-vector increment and load level increment in step k , $\Delta \mathbf{a}^k =$
 217 $\mathbf{a}^k - \mathbf{a}^{k-1}$ and $\Delta \lambda^k = \lambda^k - \lambda^{k-1}$, are computed using Newton-Raphson iter-
 218 ations. As a starting vector and load level for these iterations the solution
 219 to the previous step is used: $\mathbf{a}_0^k = \mathbf{a}^{k-1}$ and $\lambda_0^k = \lambda^{k-1}$. Subsequently, the
 220 solution vector increment is iteratively updated by $\Delta \mathbf{a}_m^k = \Delta \mathbf{a}_{m-1}^k + \delta \mathbf{a}_m^k$ and

221 $\Delta\lambda_m^k = \Delta\lambda_{m-1}^k + \delta\lambda_m^k$, where $m = 1, \dots, m_{\max}$ is the Newton-Raphson itera-
 222 tion counter. For the computation of the update vector $\delta\mathbf{a}_m^k$ and update load
 223 level $\delta\lambda_m^k$ we distinguish between the cases of force loading and displacement
 224 loading. Note that for notational brevity we omit the step number k and
 225 iteration number m in the following paragraphs ($\delta\mathbf{a}_m^k = \delta\mathbf{a}$ and $\delta\lambda_m^k = \delta\lambda$).
 226 All matrices and vectors are evaluated at the state $(\mathbf{a}_{m-1}^k, \lambda_{m-1}^k) = (\mathbf{a}, \lambda)$,
 227 *i.e.* the solution computed after $m - 1$ iterations.

228 *Force loading.* The external force vector in the discrete equilibrium equations
 229 (6) is then given by $\mathbf{f}_{\text{ext}} = \lambda\mathbf{f}$ and the constraints are imposed by $\mathbf{a} = \mathbf{C}\mathbf{a}_f + \mathbf{a}_p$,
 230 where both the matrix \mathbf{C} and the vector \mathbf{a}_p are constant throughout the
 231 simulation. The solution update is then computed through

$$\begin{pmatrix} \delta\mathbf{a}_f \\ \delta\lambda \end{pmatrix} = \begin{bmatrix} \mathbf{C}^T\mathbf{K}(\mathbf{a})\mathbf{C} & -\mathbf{C}^T\hat{\mathbf{f}} \\ \mathbf{h}^T(\mathbf{a})\mathbf{C} & q \end{bmatrix}^{-1} \begin{pmatrix} \mathbf{C}^T [\lambda\hat{\mathbf{f}} - \mathbf{f}_{\text{int}}(\mathbf{a})] \\ -\zeta(\mathbf{a}) \end{pmatrix} \quad (12)$$

232 and $\delta\mathbf{a} = \mathbf{C}\delta\mathbf{a}_f$. We compute the solution to this augmented system by
 233 solving through the Sherman-Morrison procedure discussed in *e.g.* Ref. [17].
 234 The two linear systems of equations encountered in this procedure are solved
 235 using a GMRES solver with sparse ILU pre-conditioning. Since both systems
 236 have the same left-hand-side, the pre-conditioner needs to be computed only
 237 once per Newton iteration.

238 *Displacement loading.* In this case the external force vector in equation (6)
 239 is equal to zero, and the constraints depend on the load level: $\mathbf{a} = \mathbf{C}\mathbf{a}_f +$
 240 $\mathbf{a}_p + \lambda\hat{\mathbf{a}}$. Note that the vector \mathbf{a}_p accounts for Dirichlet constraints that are
 241 not dependent on the load level λ . The solution update is then obtained by

$$\begin{pmatrix} \delta\mathbf{a}_f \\ \delta\lambda \end{pmatrix} = \begin{bmatrix} \mathbf{C}^T\mathbf{K}(\mathbf{a})\mathbf{C} & \mathbf{C}^T\mathbf{K}(\mathbf{a})\hat{\mathbf{a}} \\ \mathbf{h}^T(\mathbf{a})\mathbf{C} & \mathbf{h}^T(\mathbf{a})\hat{\mathbf{a}} + q \end{bmatrix}^{-1} \begin{pmatrix} -\mathbf{C}^T\mathbf{f}_{\text{int}}(\mathbf{a}) \\ -\zeta(\mathbf{a}) \end{pmatrix} \quad (13)$$

242 and $\delta\mathbf{a} = \mathbf{C}\delta\mathbf{a}_f + \delta\lambda\hat{\mathbf{a}}$. As for the case of force loading we apply a Sherman-
 243 Morrison procedure to solve this augmented system of equations.

244 3.3.2. The convergence criterion

After each Newton-Raphson iteration, convergence is checked based on
 the residual of the displacement field solution and phase-field solution, *i.e.*
 the solution is accepted when

$$\|\mathbf{r}^u(\mathbf{a}_m^k)\| \leq \epsilon^u \|\mathbf{r}^u(\mathbf{a}_1^k)\| \quad \text{and} \quad \|\mathbf{r}^d(\mathbf{a}_m^k)\| \leq \epsilon^d \|\mathbf{r}^d(\mathbf{a}_1^k)\|, \quad (14)$$

245 where ϵ^u and ϵ^d are tolerances for the displacement residual \mathbf{r}^u and phase-
 246 field residual \mathbf{r}^d , respectively.

247 3.3.3. The control selection procedure and restarting procedure

248 Consider the sensitivity of the load level to the path-following parameter:

$$\frac{\partial \lambda}{\partial \tau} = \dot{\Gamma}_{l_c} \left(\mathbf{h} \cdot \frac{\partial \mathbf{a}}{\partial \lambda} \right)^{-1} = \dot{\Gamma}_{l_c} \left(\mathbf{h}^d \cdot \frac{\partial \mathbf{a}^d}{\partial \lambda} \right)^{-1}. \quad (15)$$

249 From this expression it is evident that the path-following constraint will fail if
 250 the vector \mathbf{h} in equation (10) is orthogonal to the sensitivity of the solution
 251 vector. One particular situation in which this occurs is when there is no
 252 damage present at all, and hence $\|\mathbf{h}\| = 0$. This is, however, not the only
 253 situation in which problems occur. Also in the case that the phase field is
 254 rather insensitive to the load level ($\|\partial \mathbf{a}^d / \partial \lambda\| \approx 0$), the constraint equation
 255 fails. This situation is encountered in the case that elastic behavior occurs,
 256 which happens particularly in the cases of initial loading and unloading. For
 257 this reason, initially displacement control is used. The switch to the fracture-
 258 surface area constraint is made after a significant amount of fracture-surface
 259 area has been formed.

260 Depending on the number of Newton-Raphson iterations the path-parameter
 261 increment is adjusted [16]. To this end a target number of Newton-Raphson
 262 iterations, m_{targ} , is specified. The path-parameter for the next increment is
 263 then scaled with a factor m_{targ}/m with a maximum of $\Delta\tau_{\text{max}}$. Evidently,
 264 when the path-parameter increment is chosen too large, it can occur that the
 265 Newton-Raphson iterations do not converge within m_{max} iterations. In that
 266 case the Newton-Raphson procedure for the same step is repeated with the
 267 path-parameter increment scaled by $m_{\text{targ}}/m_{\text{max}}$.

268 4. Fracture-controlled staggered solution procedure

269 Taking the monolithic path-following procedure in Algorithm 1 for the
 270 case of displacement loading ($\mathbf{a}_p = \lambda \hat{\mathbf{a}}$) as a starting point, we derive a stag-
 271 gered path-following procedure. The most notable difference of this stag-
 272 gered algorithm compared to the monolithic Algorithm 1 is that no Newton-
 273 Raphson iterations are conducted and that the associated convergence crite-
 274 rion is omitted. A consequence of this is that an additional source of error
 275 is introduced in the staggered scheme, which, in practice, needs to be com-
 276 pensated for by using smaller load step sizes. By virtue of the fact that no

277 (Newton) iterations are performed within a single time step, this staggered
 278 approach is, however, considerably faster per load step than the Newton
 279 procedure.

```

Input:  $(\mathbf{a}^0, \lambda^0), \mathcal{H}^0$  #State vector, load level & history field
Output:  $(\mathbf{a}^1, \lambda^1), (\mathbf{a}^2, \lambda^2), \dots, (\mathbf{a}^{n_{\text{steps}}}, \lambda^{n_{\text{steps}}})$  #Discrete eq. path

#Initialization
control = 'displacement'

#Load steps
for  $k = 1, \dots, n_{\text{steps}}$  :
     $\mathbf{a}^k, \lambda^k = \text{staggered\_solution\_update}(\mathbf{a}^{k-1}, \lambda^{k-1}, \mathcal{H}^{k-1}, \left. \frac{\partial \mathcal{H}}{\partial \lambda} \right|^{k-1},$ 
    control)
     $\mathcal{H}^k, \left. \frac{\partial \mathcal{H}}{\partial \lambda} \right|^k = \text{update\_history\_field}(\mathbf{a}^k, \mathcal{H}^{k-1})$ 
    control = select_control_equation( $\mathbf{a}^k, \mathcal{H}^k$ )
end
  
```

Algorithm 2: Staggered path-following procedure

280 The staggered procedure developed herein is outlined in Algorithm 2. In
 281 the following sections we study the `staggered_solution_update` procedure.
 282 In Section 4.1 we show how the displacement-controlled staggered procedure
 283 as proposed by Miehe *et al.* [2] follows as a simplification of the incremental-
 284 iterative procedure in the previous section. This procedure is employed in
 285 the initial stage of loading, when fracture propagation does not yet occur.
 286 In Section 4.2 the staggered fracture-controlled path-following procedure is
 287 derived as a simplification of the monolithic fracture-controlled procedure
 288 outlined in the previous section.

289 Note that in Algorithm 2 the sensitivity of the history field with respect
 290 to the load parameter is evaluated along with the history field itself at the
 291 end of each load step. Evaluation of this sensitivity is required at the end of
 292 step k for the staggered fracture-controlled procedure and is given by

$$\left. \frac{\partial \mathcal{H}}{\partial \lambda} \right|^k = \begin{cases} \left. \frac{\partial \psi_e^+}{\partial \boldsymbol{\varepsilon}} \right|^k : \hat{\boldsymbol{\varepsilon}} & \psi_e^+(\boldsymbol{\varepsilon}^k) \geq \mathcal{H}^{k-1} \\ 0 & \text{otherwise} \end{cases}, \quad (16)$$

where $\hat{\boldsymbol{\varepsilon}} = \nabla^s \left(\sum_{I=1}^{n_u} \mathbf{N}_I^u(\mathbf{x}) \frac{\partial a_I^u}{\partial \lambda} \right)$ is the strain field sensitivity to the load

level λ , with:

$$\mathbf{K} \frac{\partial \mathbf{a}}{\partial \lambda} = \mathbf{0} \quad \text{and constraint} \quad \frac{\partial \mathbf{a}}{\partial \lambda} = \mathbf{C} \frac{\partial \mathbf{a}_f}{\partial \lambda} + \hat{\mathbf{a}}. \quad (17)$$

293 In order to simplify notation, in the following sections we drop the super-
 294 script k indicating the load step. Instead, the initial state for a given load
 295 step is indicated by a subscript 0 (following the notation for the Newton-
 296 Raphson initial estimate) and the updated state is represented without sub-
 297 or superscripts, *i.e.* $\mathbf{a} = \mathbf{a}_0 + \Delta \mathbf{a}$ and $\lambda = \lambda_0 + \Delta \lambda$.

298 4.1. Displacement-controlled staggered procedure

A displacement-controlled simulation can be cast into the form of a path-
 following procedure by using the control equation $\zeta = \Delta \lambda - \dot{\lambda} \Delta \tau$ (and $\mathbf{a}_p =$
 $\lambda \hat{\mathbf{a}}$), from which it follows that $\mathbf{h} = \mathbf{0}$ and $q = 1$. The monolithic augmented
 system of equations (13) for the Newton-Raphson iterations is then given by

$$\begin{bmatrix} \mathbf{K}^{uu} & \mathbf{K}^{ud} & \mathbf{0} \\ \mathbf{K}^{du} & \mathbf{K}^{dd} & \mathbf{0} \\ \mathbf{0}^T & \mathbf{0}^T & 1 \end{bmatrix} \begin{pmatrix} \delta \mathbf{a}^u \\ \delta \mathbf{a}^d \\ \delta \lambda \end{pmatrix} = \begin{pmatrix} -\mathbf{f}_{\text{int}}^u \\ -\mathbf{f}_{\text{int}}^d \\ \dot{\lambda} \Delta \tau \end{pmatrix}, \quad (18)$$

299 with the constraints $\delta \mathbf{a}^u = \mathbf{C}^u \delta \mathbf{a}_f^u + \delta \lambda \hat{\mathbf{a}}^u$ and $\delta \mathbf{a}^d = \mathbf{C}^d \delta \mathbf{a}_f^d$, where the
 300 constraints matrix \mathbf{C} has been decomposed in a displacement part \mathbf{C}^u and a
 301 phase-field part \mathbf{C}^d .

The system (18) can serve as the starting point for the derivation of a
 displacement-controlled staggered procedure. To this end, the updates after
 a single iteration are accepted as the solution increments, *i.e.* $\Delta \mathbf{a} = \delta \mathbf{a}$ and
 $\Delta \lambda = \delta \lambda$. An approximate solution to the system is then obtained in three
 steps. In Step 1 the phase-field sub-problem is solved with the load level,
 displacement field and history field resulting from the previous load step.
 In Step 2 the load level is updated, and finally in Step 3 the displacement
 sub-problem is solved with the phase field as computed in Step 1 and the
 load level as determined in Step 2. These three sub-problems can be written
 in total form as:

$$\mathbf{K}^{dd}(\mathcal{H}_0) \mathbf{a}^d = -\mathbf{f}_{\text{int}}^d(\mathbf{a}_0^d, \mathcal{H}_0) + \mathbf{K}^{dd}(\mathcal{H}_0) \mathbf{a}_0^d \quad \mathbf{a}^d = \mathbf{C}^d \mathbf{a}_f^d + \mathbf{a}_p^d \quad (19a)$$

$$\lambda = \lambda_0 + \dot{\lambda} \Delta \tau \quad (19b)$$

$$\mathbf{K}^{uu}(\mathbf{a}_0^u, \mathbf{a}^d) \mathbf{a}^u = -\mathbf{f}_{\text{int}}^u(\mathbf{a}_0^u, \mathbf{a}^d) + \mathbf{K}^{uu}(\mathbf{a}_0^u, \mathbf{a}^d) \mathbf{a}_0^u \quad \mathbf{a}^u = \mathbf{C}^u \mathbf{a}_f^u + \mathbf{a}_p^u + \lambda \hat{\mathbf{a}}^u \quad (19c)$$

302 Further simplification using

$$\mathbf{f}_{\text{int}}^d(\mathbf{0}, \mathcal{H}_0) = \mathbf{f}_{\text{int}}^d(\mathbf{a}_0^d, \mathcal{H}_0) - \mathbf{K}^{dd}(\mathcal{H}_0)\mathbf{a}_0^d = -2 \int_{\Omega} \mathcal{H}_0 \mathbf{N}^d dV \quad (20)$$

303 and $\mathbf{f}_{\text{int}}^u(\mathbf{a}_0^u, \mathbf{a}_0^d) = \mathbf{K}^{uu}(\mathbf{a}_0^u, \mathbf{a}_0^d)\mathbf{a}_0^u$ finally results in the *control* == 'displacement'
 304 conditional block in the `staggered_solution_update` function shown in Al-
 305 gorithm 3. We note that this algorithm is equivalent to the staggered algo-
 306 rithm presented in Ref. [2].

307 4.2. Fracture-controlled staggered procedure

Using the fracture control equation (9), the monolithic augmented system of equations (13) for the Newton-Raphson iterations can be written as

$$\begin{bmatrix} \mathbf{K}^{uu} & \mathbf{K}^{ud} & \mathbf{0} \\ \mathbf{K}^{du} & \mathbf{K}^{dd} & \mathbf{0} \\ \mathbf{0}^T & \mathbf{h}^{dT} & 0 \end{bmatrix} \begin{pmatrix} \delta \mathbf{a}_f^u \\ \delta \mathbf{a}_f^d \\ \delta \lambda \end{pmatrix} = \begin{pmatrix} -\mathbf{f}_{\text{int}}^u \\ -\mathbf{f}_{\text{int}}^d \\ \dot{\Gamma}_{l_c} \Delta \tau \end{pmatrix}, \quad (21)$$

308 with the constraints $\delta \mathbf{a}^u = \mathbf{C}^u \delta \mathbf{a}_f^u + \delta \lambda \hat{\mathbf{a}}^u$ and $\delta \mathbf{a}^d = \mathbf{C}^d \delta \mathbf{a}_f^d$, and with \mathbf{h}^d as
 309 defined in equation (10).

Following the same procedure as for the case of staggered displacement control, the updates of the state vector and load level after a single Newton-Raphson iteration are accepted as the solution increments, *i.e.* $\Delta \mathbf{a} = \delta \mathbf{a}$ and $\Delta \lambda = \delta \lambda$. In contrast to the case of displacement control discussed in the previous section, in this case there is no natural decoupling of the phase-field and the load level. An approximate solution to the system (21) is therefore obtained in only two steps. In Step 1 the combined phase field and load level system is solved, with the displacement field and history field following from the previous load step. In Step 2 the displacement sub-problem is solved with the phase field and load level as computed in Step 1. In total form, this results in the following sub-problems:

$$\begin{bmatrix} \mathbf{K}^{dd}(\mathcal{H}_0) & -\hat{\mathbf{f}}^d(\mathbf{a}_0^d, \frac{\partial \mathcal{H}}{\partial \lambda}|_0) \\ \mathbf{h}^d(\mathbf{a}_0^d)^T & 0 \end{bmatrix} \begin{pmatrix} \mathbf{a}^d \\ \lambda \end{pmatrix} = \begin{pmatrix} -\mathbf{f}_{\text{int}}^d(\mathbf{0}, \mathcal{H}_0) - \lambda_0 \hat{\mathbf{f}}^d(\mathbf{a}_0^d, \frac{\partial \mathcal{H}}{\partial \lambda}|_0) \\ \dot{\Gamma}_{l_c}(\tau - \tau_0) + \mathbf{h}^d(\mathbf{a}_0^d)^T \mathbf{a}_0^d \end{pmatrix} \quad (22a)$$

$$\mathbf{K}^{uu} \mathbf{a}^u = -\mathbf{f}_{\text{int}}^u + \mathbf{K}^{uu} \mathbf{a}_0^u \quad (22b)$$

310 with $\mathbf{a}^d = \mathbf{C}^d \mathbf{a}_f^d + \mathbf{a}_p^d$ and $\mathbf{a}^u = \mathbf{C}^u \mathbf{a}_f^u + \mathbf{a}_p^u + \lambda \hat{\mathbf{a}}^u$ and where the unit driving
 311 force is defined as

$$\begin{aligned} \hat{\mathbf{f}}^d(\mathbf{a}_0^d, \frac{\partial \mathcal{H}}{\partial \lambda} |_0) &= -\mathbf{K}^{du}(\mathbf{a}_0^d, \frac{\partial \mathcal{H}}{\partial \boldsymbol{\varepsilon}} |_0) \hat{\mathbf{a}}^u = \int_{\Omega} 2(1 - d_0) \mathbf{N}^d (\hat{\boldsymbol{\varepsilon}} : \frac{\partial \mathcal{H}}{\partial \boldsymbol{\varepsilon}} |_0) dV \\ &= \int_{\Omega} 2(1 - d_0) \mathbf{N}^d \frac{\partial \mathcal{H}}{\partial \lambda} |_0 dV. \end{aligned} \quad (23)$$

312 Using the fact that $\mathbf{h}^{dT} \mathbf{a}_0^d = 2\dot{\Gamma}_{l_c} \tau_0$ this results in the *control* == 'fracture'
 313 conditional block in the procedure shown in Algorithm 3. The augmented
 314 system of equations (22a) is solved using the Sherman-Morrison procedure.

315 5. Numerical simulations

316 In this section the performance of the numerical algorithms outlined in
 317 the previous sections is studied. We will investigate the proposed numeri-
 318 cal algorithms using two standard benchmark simulations: the single edge
 319 notched tension test (Section 5.1) and the single edge notched pure shear
 320 test (Section 5.2). Moreover, we will study the performance of the mono-
 321 lithic and staggered schemes for a tension test with multiple pre-existing
 322 fractures (Section 5.3). In contrast to the two benchmark tests, this simula-
 323 tion demonstrates the performance of the algorithms in the case of fracture
 324 interactions.

325 For all simulations we assume plane strain conditions. The first Lamé
 326 parameter is taken as $\lambda = 121.15 \text{ kN/mm}^2$, while the second Lamé parameter
 327 (or shear modulus) is $\mu = 80.77 \text{ kN/mm}^2$. The critical energy release rate
 328 equals $\mathcal{G}_c = 2.7 \cdot 10^{-3} \text{ kN/mm}$.

329 5.1. Single edge notched tension test

330 We consider a two-dimensional square specimen of size $1 \times 1 \text{ mm}^2$ with
 331 a horizontal notch starting at the left boundary and ending in the middle
 332 of the specimen (Figure 2a). The bottom boundary is constrained in the
 333 vertical direction and is free to move in the horizontal direction. In order to
 334 eliminate rigid body motions, the bottom-left corner point is also constrained
 335 in horizontal direction. The top boundary is stretched in vertical direction,
 336 and free to move horizontally. For all simulations in this section the phase-
 337 field length scale is taken as $l_c = 0.015 \text{ mm}$. Linear triangular meshes for
 338 both the displacement field and phase field have been used, with local mesh

```

def staggered_solution_update (  $\mathbf{a}_0$ ,  $\lambda_0$ ,  $\mathcal{H}_0$ ,  $\frac{\partial \mathcal{H}}{\partial \lambda} \Big|_0$ , control ):
    #Update the phase field and load level
     $\mathbf{K}^{dd}, \mathbf{f}_{\text{int}}^d = \text{assemble\_phasefield\_system}(\mathbf{0}, \mathcal{H}_0)$ 
    if control == 'displacement' :
        #Solve the phase-field system
         $\mathbf{K}^{dd} \mathbf{a}^d = -\mathbf{f}_{\text{int}}^d$  with  $\mathbf{a}^d = \mathbf{C}^d \mathbf{a}_f^d + \mathbf{a}_p^d$ 
        #Update the load level
         $\lambda = \lambda_0 + \dot{\lambda} \Delta \tau$ 
    else if control == 'fracture' :
         $\hat{\mathbf{f}}^d = \text{assemble\_drivingforce}(\mathbf{a}_0^d, \frac{\partial \mathcal{H}}{\partial \lambda} \Big|_0)$ 
        #Solve the fracture-controlled phase-field system
        
$$\begin{bmatrix} \mathbf{K}^{dd} & -\hat{\mathbf{f}}^d \\ \mathbf{h}^{dT} & 0 \end{bmatrix} \begin{pmatrix} \mathbf{a}^d \\ \lambda \end{pmatrix} = \begin{pmatrix} -\mathbf{f}_{\text{int}}^d - \lambda_0 \hat{\mathbf{f}}^d \\ \dot{\Gamma}_{l_c}(\tau_0 + \tau) \end{pmatrix}$$
 with  $\mathbf{a}^d = \mathbf{C}^d \mathbf{a}_f^d + \mathbf{a}_p^d$ 
    end
    #Update the displacement field
     $\mathbf{K}^{uu} = \text{assemble\_elasticity\_system}(\mathbf{a}_0^u, \mathbf{a}^d)$ 
    #Solve the elasticity system
     $\mathbf{K}^{uu} \mathbf{a}^u = \mathbf{0}$  with  $\mathbf{a}^u = \mathbf{C}^u \mathbf{a}_f^u + \mathbf{a}_p^u + \lambda \hat{\mathbf{a}}^u$ 
    return  $\mathbf{a}$ ,  $\lambda$ 
end

```

Algorithm 3: Staggered solution update procedure

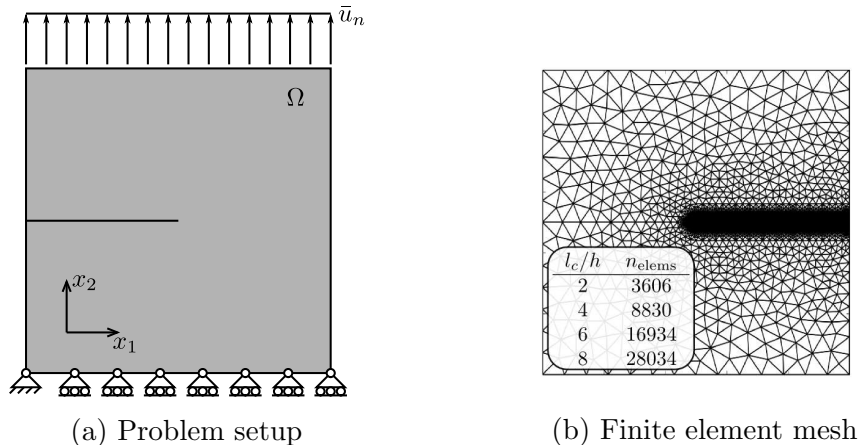


Figure 2: Problem setup and finite element mesh for the single edge notched tension test.

339 refinement along the anticipated crack path. The number of elements for the
 340 various meshes is reported in Figure 2b, where h is the characteristic element
 341 size in the refinement region.

342 Below we will study the performance of three solution algorithms for
 343 this test case: the displacement-controlled staggered scheme as employed in
 344 *e.g.* Ref. [2], the fracture-controlled Newton-Raphson scheme as outlined in
 345 Section 3, and the fracture-controlled staggered scheme proposed in Section 4.

346 5.1.1. Displacement-controlled staggered scheme

347 In this subsection we consider the solution obtained by the displacement-
 348 based staggered solution procedure as proposed by Miehe *et al.* [2]. The mo-
 349 tivation for considering this solution procedure is to study the dependence of
 350 the solution on the selected displacement increment size and to enable direct
 351 comparison with fracture-controlled schemes. This study provides insight in
 352 the performance of staggered solution procedures compared to the monolithic
 353 scheme considered in this work.

354 In Figure 3 we study the influence of the mesh size by consideration of
 355 meshes with characteristic element sizes of $h = l_c/2, l_c/4, l_c/6$ and $l_c/8$ in
 356 the region where the crack is anticipated to propagate. For all simulations
 357 a relatively large step size of $\Delta \bar{u}_n = 1 \cdot 10^{-5}$ mm is used. Figures 3a and
 358 3b depict the dependence of the response on the selected mesh size. As
 359 observed, the measured response converges upon mesh refinement. Based on
 360 these observations, in the remainder of this section we will employ a fixed

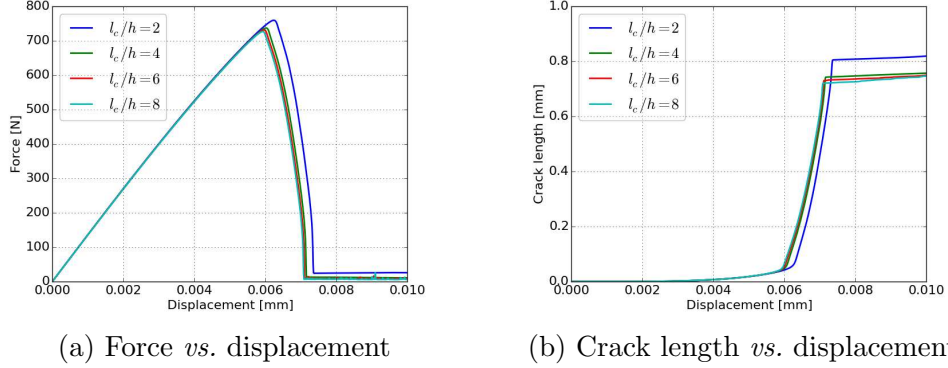
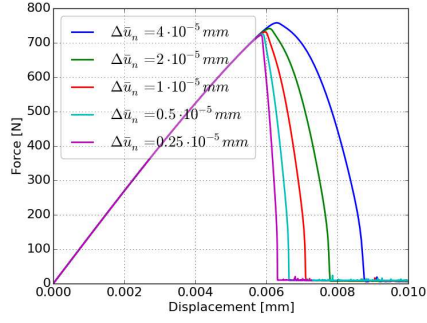


Figure 3: Mesh convergence study for the single edge notched tension test solved with the displacement-controlled staggered solution algorithm.

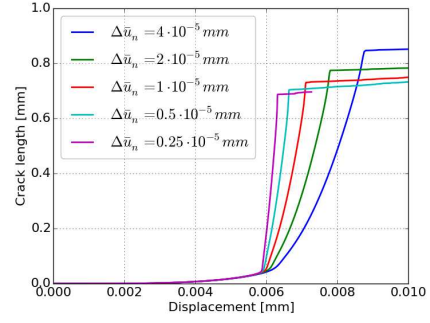
361 mesh size with a characteristic element size of $h = l_c/6$ in the refinement
 362 region.

363 In Figure 4 we study the dependence of the response on the selected step
 364 size, $\Delta\bar{u}_n$. From the force-displacement curves we observe that the overall
 365 dissipation is overestimated when using too large step sizes. On one hand
 366 this is explained by the fact that a too large step size delays the instance
 367 of propagation, *i.e.* the phase field reaches a value of 1 at a later moment
 368 than for a smaller step size (Figure 4c). On the other hand we observe that
 369 the overall crack length is considerably overestimated for too large step sizes
 370 (Figure 4b). In Figure 5 we illustrate the primary reason for this overes-
 371 timation by considering the phase field at $\Gamma_{l_c} \approx 0.4$ mm for step sizes of
 372 $\Delta\bar{u}_n = 4 \cdot 10^{-5}$ mm and $\Delta\bar{u}_n = 0.5 \cdot 10^{-5}$ mm. As can be seen, the delay in
 373 the update of the phase field due to the use of the staggered solution pro-
 374 cedure causes the crack to widen, and hence the total fracture length (Γ_{l_c}
 375 at $\bar{u}_n = 0.009$ mm) to be overestimated. In Table 1 we report the computed
 376 peak force values (F_{peak}) and its corresponding displacement ($\bar{u}_{n,\text{peak}}$), as well
 377 as the crack length at $\bar{u}_n = 0.009$ mm (Γ_{ult}). From the results in Table 1 it
 378 can be inferred that all reported quantities converge linearly under step size
 379 refinement.

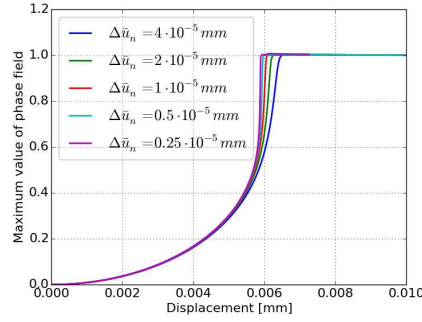
380 Evidently, using uniform step sizes is not optimal in terms of computa-
 381 tional effort versus step size error. For example, relatively large step sizes can
 382 be used in the elastic regime. As we will see in Section 5.1.3, the fracture-
 383 based scheme provides a natural adaptive refinement strategy.



(a) Force *vs.* displacement



(b) Crack length *vs.* displacement

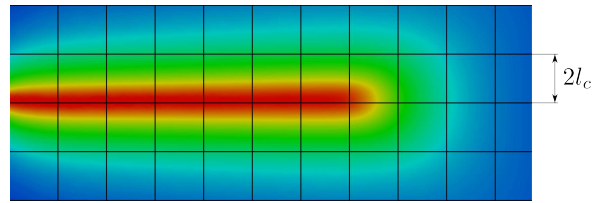


(c) Maximum phase field value *vs.* displacement

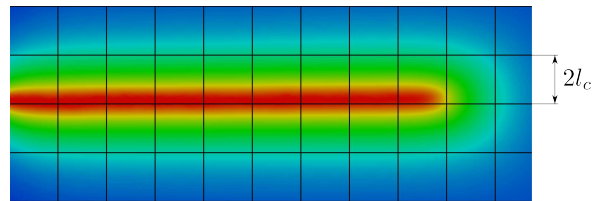
Figure 4: Step size study for the single edge notched tension test solved with the displacement-controlled staggered solution algorithm.

$\Delta \bar{u}_n$ [mm]	F_{peak} [N]	$\bar{u}_{n,\text{peak}}$ [mm]	Γ_{ult} [mm]
$4 \cdot 10^{-5}$	758.0	0.00628	0.848
$2 \cdot 10^{-5}$	741.3	0.00608	0.780
$1 \cdot 10^{-5}$	731.4	0.00597	0.742
$0.5 \cdot 10^{-5}$	725.6	0.00589	0.723

Table 1: Dependence of various solution characteristics on the step size for the single edge notched tension test with the displacement-controlled staggered scheme.



(a) $\Delta\bar{u}_n = 4 \cdot 10^{-5}$ mm



(b) $\Delta\bar{u}_n = 0.5 \cdot 10^{-5}$ mm

Figure 5: Phase field at fracture length $\Gamma_{l_c} \approx 0.4$ mm for the single edge notched tension test. Note that the plotted grid is merely a visual aid, and is not related to the finite element mesh.

384 *5.1.2. Fracture-controlled monolithic scheme*

385 In this section we study the monolithic fracture-controlled scheme (Al-
 386 gorithm 1) with and without adaptive crack size increments. As outlined in
 387 Section 3.3.3, we use displacement control to initiate the solution procedure.
 388 In this case $\Delta\bar{u}_n = 1 \cdot 10^{-4}$ mm is used. When the crack length increment
 389 exceeds $\Delta\Gamma_{\text{switch}} = 1 \cdot 10^{-5}$ mm, the switch is made to fracture control. This
 390 choice for $\Delta\Gamma_{\text{switch}}$ is based on the fact that it should be considerably larger
 391 than the machine precision, and considerably smaller than the representa-
 392 tive element size h , since the switch to fracture control should be made well
 393 before the fracture starts to propagate. The obtained solution was observed
 394 to be insensitive to variations in this switching value.

395 In Figure 6a we show the force-displacement curves for the case in which
 396 the fracture surface increment $\Delta\Gamma$ is kept fixed. We observe that for all sim-
 397 ulations the Newton-Raphson procedure with a tolerance of 1×10^{-5} fails to
 398 converge at some point in the incrementation process after softening and/or
 399 snapback has occurred. This is caused by the fact that the initial estimate
 400 for the Newton procedure is outside the radius of convergence of the Newton
 401 procedure. In line with this is the observation that decreasing the step size
 402 increases – albeit moderately – the extend to which the equilibrium path

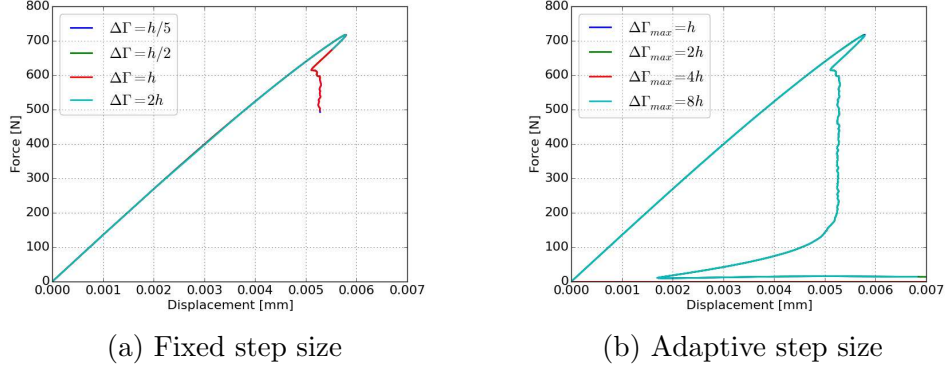


Figure 6: Fracture-controlled Newton-Raphson solutions for the single edge notched tension test.

403 can be computed. A notable difference between these monolithic results and
 404 the staggered results presented above is that the errors due to the staggered
 405 steps are completely eliminated, *i.e.* virtually the same result is obtained
 406 independent of the selected crack length increment.

407 In order to track the complete equilibrium path we have employed the
 408 adaptive scheme as discussed in Section 3.3.3 with $m_{\text{targ}} = 4$. The results
 409 are presented in Figure 6b. With this adaptive step size increment, the same
 410 equilibrium path is recovered regardless of the maximum allowable increment.
 411 In fact, the maximum step size increment is ineffective as a result of the
 412 limitation imposed by the target number of Newton iterations. We observe
 413 that the monolithic solution procedure is very effective in capturing the peak
 414 load. The computed value of $F_{\text{peak}} = 715.26 \text{ N}$ is free of the step size errors
 415 introduced by the staggered procedure in Section 5.1.1, and can be obtained
 416 in relatively few steps. In addition, the fracture-controlled Newton scheme
 417 is capable of tracking the snap-back part of the equilibrium path.

418 The origin of this snap-back behavior is that at the crack tip a phase
 419 field needs to nucleate. In the case that we enrich the tip of the pre-existing
 420 fracture with a phase field (see Appendix C) – thereby regularizing the stress
 421 field around the tip – this snap-back feature vanishes (Figure 7).

422 5.1.3. Fracture-controlled staggered scheme

423 As for the monolithic scheme discussed above, for the fracture-controlled
 424 staggered scheme we use an initial displacement step size of $\Delta \bar{u}_n = 1 \cdot 10^{-4} \text{ mm}$
 425 and switch to the fracture-controlled scheme when the crack length increment

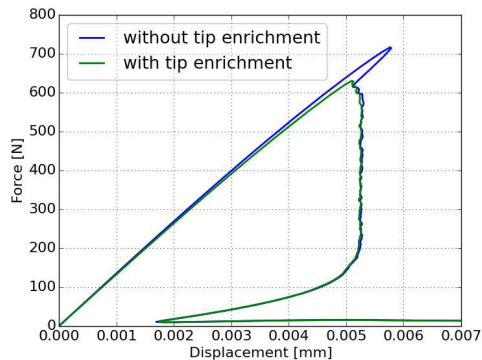


Figure 7: Comparison of the equilibrium path computed using the monolithic fracture-controlled scheme with and without tip enrichment.

426 exceeds $\Delta\Gamma_{\text{switch}} = 1 \cdot 10^{-5}$ mm. In Figure 8 the results are shown for various
 427 crack length increments, and some solution characteristics are collected in
 428 Table 2.

429 It is observed that as for the displacement-controlled staggered solution
 430 procedure, an error is introduced by this staggered scheme. For the quantities in Table 2 this error is observed to decrease at least linearly with the
 431 selected step size. Compared to the displacement-based scheme, the fracture-
 432 controlled staggered scheme has two advantages. First, under step-size re-
 433 finement it converges to the Newton-Raphson solution, including snap-back
 434 behavior. Such convergence is not observed for the displacement-based stag-
 435 gered scheme of Section 5.1.1. A second advantage is that the step size for
 436 the fracture controlled simulation can be selected conveniently by relating
 437 it to the representative element size (h). This permits us to allow for the
 438 gradual motion of a crack through the mesh, *i.e.* the crack is not permitted
 439 to propagate through multiple elements in a single step when $\Delta\Gamma$ is limited
 440 by the element size. As indicated above, the fracture-controlled procedure
 441 serves as an automatic displacement step size adjuster. This is shown in Fig-
 442 ure 9 where the displacement step size is plotted versus the step size number.
 443 As can be seen, the staggered scheme automatically accounts for a smaller
 444 (or even negative) displacement increment when crack propagation occurs.
 445

446 In Table 2 we also compare the monolithic scheme with adaptive step size
 447 with the staggered scheme for various step sizes. We observe that the mono-
 448 lithic scheme on average has a step size, $\Delta\Gamma$, comparable to the staggered
 449 scheme with $\Delta\Gamma = \frac{1}{2}h$. Also the number of steps to track the shown equilib-

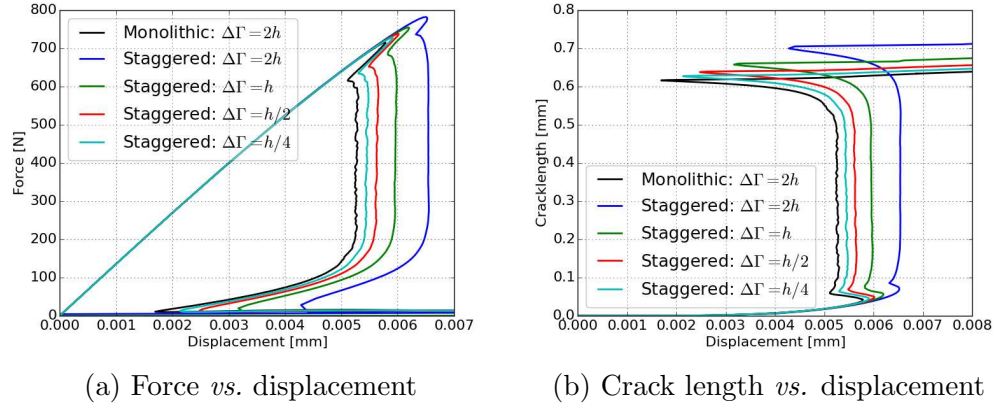


Figure 8: Fracture-controlled staggered solutions for the single edge notched tension specimen with various crack length increments.

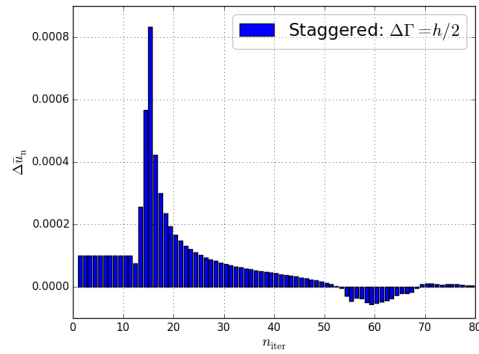


Figure 9: Variation of the displacement increment over the fracture-controlled staggered iterations for first 80 steps.

Scheme	$\Delta\Gamma$ ($\times h$)	n_{steps}	n_{iter}	n_{solve}	F_{peak} [N]	$\bar{u}_{n,\text{peak}}$ [mm]	$\bar{u}_{n,\text{snap}}$ [mm]	Γ_{ult} [mm]
Monolithic	0.52 (0.64)	488	2.48 (1.56)	1210	716.8	0.00579	0.00525	0.639
Staggered	2	150	1	150	782.3	0.00651	0.00654	0.717
Staggered	1	275	1	275	754.9	0.00618	0.00597	0.676
Staggered	$\frac{1}{2}$	529	1	529	738.0	0.00599	0.00565	0.657
Staggered	$\frac{1}{4}$	1235	1	1235	728.8	0.00590	0.00530	0.647

Table 2: Comparison of the monolithic and staggered path-following schemes for the tension simulation. For the monolithic scheme the mean value and standard deviation (in brackets) are given when applicable.

450 rium path is similar (488 for the monolithic scheme *vs.* 529 for the staggered
451 scheme), but evidently the number of linear system solves for the monolithic
452 scheme is considerably higher (1210 for the monolithic scheme *vs.* 529 for
453 the staggered scheme) and in addition each system solve in the monolithic
454 scheme is computationally more expensive. The error related to the stag-
455 gered procedure remains limited to a few percent for both the peak load and
456 the overall crack length. When comparing with the displacement-controlled
457 staggered scheme with $\Delta\bar{u}_n = 2 \cdot 10^{-5}$ mm (Table 1), for which a similar num-
458 ber of system solves is required (500), we observe that the fracture-controlled
459 staggered scheme provides a better approximation of the peak load and total
460 crack length than the displacement-controlled scheme. For the peak load the
461 obtained improvement is moderate, and can be attributed to the fact that the
462 fracture-controlled scheme automatically provides displacement step size ad-
463 justments. A significant improvement is obtained for the total crack length,
464 which is a consequence of the fact that the displacement-controlled scheme
465 fails to account for the snap-back behavior. For the staggered scheme with
466 $\Delta\Gamma = \frac{1}{4}h$ a similar number of system solves is required as for the monolithic
467 scheme. In this case errors of less than 2% in the peak load and crack length
468 are obtained.

469 5.2. Single edge notched pure shear test

470 In this section we investigate the setup represented in Figure 10a. The
471 geometry is identical to that considered for the tension simulation discussed
472 above, but pure shear boundary conditions are used. This means that the
473 vertical displacement component is constrained on all four sides of the do-
474 main. Moreover, the bottom boundary is constrained horizontally, and a
475 prescribed horizontal displacement, \bar{u}_s , is applied to the top boundary. The
476 same material parameters are used as for the tension simulation. The frac-
477 ture length scale is equal to $l_c = 0.015$ mm. In order to accurately capture

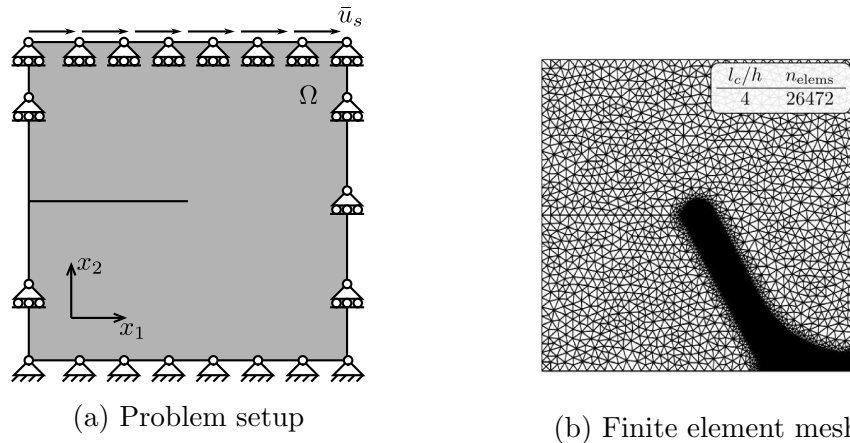


Figure 10: Problem setup and finite element mesh for the single edge notched pure shear test.

478 the phase-field evolution, the mesh is refined along the anticipated crack
 479 path (Figure 10b). The characteristic element size in this refinement region
 480 is $h = l_c/4 = 0.00375$ mm, which results in a mesh with 26472 elements.

481 In Figure 11 we study the convergence of the displacement-based stag-
 482 gered solution procedure under step size refinement. We observe very close
 483 agreement with the results reported in literature [2]. Using the fracture-
 484 controlled Newton-Raphson procedure with adaptive step size and $\Delta\Gamma_{\max} =$
 485 $2h$ (Figure 12) we observe that the bump in the force-displacement curve at
 486 crack nucleation is related to the occurrence of snap-back, a phenomenon not
 487 captured by the displacement-based staggered scheme. By comparison with
 488 the results with phase-field tip enrichment, we observe that this snap-back
 489 behavior is closely related to the nucleation of the phase-field fracture at the
 490 tip of the pre-existing fracture.

491 In Figure 13 we study the influence of the crack-length increment size
 492 for the fracture-controlled staggered solution procedure. This figure conveys
 493 that the staggered procedure converges to the monolithic result as the step
 494 size decreases. In Table 3 we compare the monolithic and staggered scheme
 495 for various quantities of interest. The total crack length Γ_{ult} is measured
 496 at $\bar{u}_s = 0.016$ mm. The peak load and total crack length are observed to
 497 converge at least at a linear rate. As for the tensile test we observe that the
 498 crack path is predicted appropriately by the staggered scheme for relatively
 499 large step sizes. For $\Delta\Gamma = h/2$ we observe errors of a few percent, while

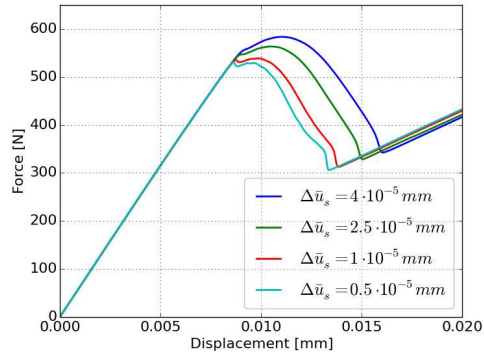


Figure 11: Step size study for the single edge notched pure shear test solved with the displacement-controlled staggered solution algorithm.

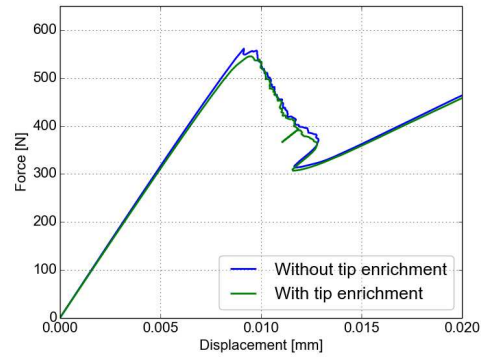


Figure 12: Comparison of the equilibrium path computed using the monolithic fracture-controlled scheme with and without tip enrichment.

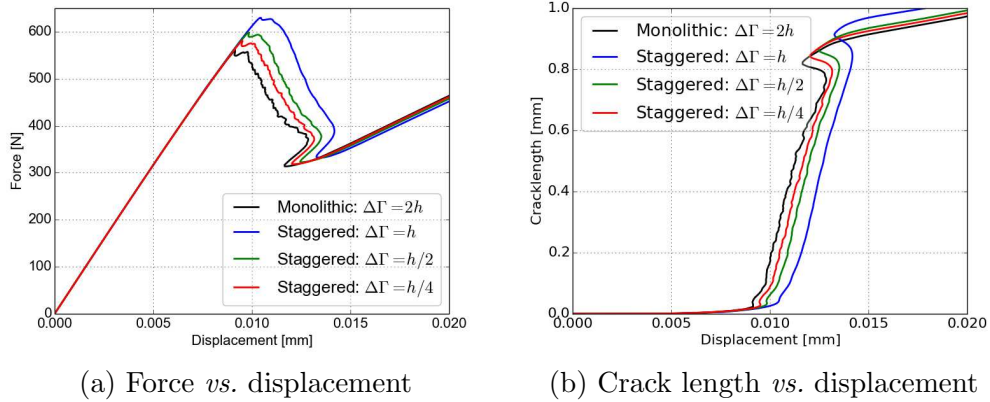


Figure 13: Fracture-controlled staggered solutions for the single edge notched shear specimen with various crack length increments.

Scheme	$\Delta\Gamma (\times h)$	n_{steps}	n_{iter}	n_{solve}	$F_{\text{peak}} [\text{N}]$	$\Gamma_{\text{ult}} [\text{mm}]$
Monolithic	1.17(0.58)	207	3.69(1.06)	764	557.2	0.93
Staggered	2	162	1	162	684.6	1.05
Staggered	1	281	1	281	629.6	0.98
Staggered	$\frac{1}{2}$	522	1	522	593.6	0.94
Staggered	$\frac{1}{4}$	1061	1	1061	575.3	0.93

Table 3: Comparison of the monolithic and staggered path-following schemes for the pure shear simulation. For the monolithic scheme the mean value and standard deviation (in brackets) are given when applicable.

500 the involved number of system solves is considerably smaller than for the
 501 monolithic scheme.

502 5.3. Multiple inclusion test

503 We finally study the performance of the fracture-based path-following
 504 schemes for a test case with complex fracture surface evolution. To this
 505 end we consider a $1 \times 1 \text{ mm}^2$ tensile test with six, randomly distributed,
 506 pre-existing cracks (Figure 14). The discretized displacement field is dis-
 507 continuous over the pre-existing cracks, which is established by aligning the
 508 elements of the bulk material with the pre-existing cracks and duplicating the
 509 nodes on the cracks. An irregular triangular finite element mesh with 28826
 510 equal-sized linear elements and 14700 nodes is used to discretize the bulk
 511 material. The element length along the boundaries and pre-existing cracks is

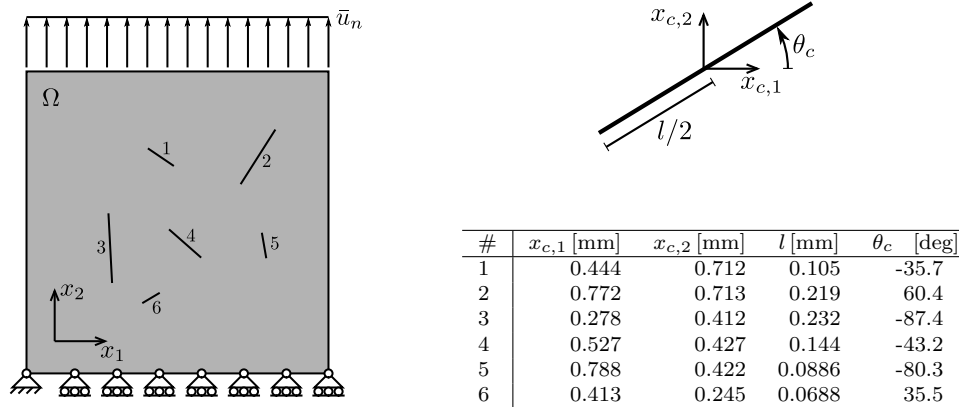


Figure 14: Schematic representation of a $1 \times 1 \text{ mm}^2$ tensile specimen with six, randomly generated, pre-existing cracks.

512 $h = 0.01 \text{ mm}$. The same material parameters as for the test cases discussed
 513 above have been used. The crack length scale is equal to $l_c = 0.025 \text{ mm}$.

514 In Figure 15 we show the solutions obtained by the monolithic scheme,
 515 with and without tip enrichment. As for the above experiments we observe
 516 overshoots in the response curve in the case that the pre-existing tips are
 517 not regularized by a phase field. This effect is here more pronounced due
 518 to the fact that the elements around the tips are relatively coarse (the same
 519 element size is used throughout the complete domain). Evidently, due to
 520 the iteration-based step size adjustment strategy, the monolithic scheme is
 521 capable of tracking the snap-back paths.

522 In Figure 16 we show six snapshots of the fracture evolution pattern.
 523 The labels (a)-(f) are reflected in the force-displacement diagram in Figure
 524 15b. Initially, the specimen is loaded elastically (a), until pre-existing crack
 525 2 propagates toward the right edge of the specimen (b). When this happens,
 526 the specimen unloads, after which a secondary crack propagates from the
 527 bottom tip of pre-existing crack 2 (c) and merges with pre-existing crack 1
 528 (d). After another unloading stage, finally pre-existing crack 1 propagates
 529 toward the left edge of the specimen (e) until it reaches the left edge and the
 530 specimen lost all its load-carrying capacity (f).

531 In Figure 17 we show the force-displacement curves computed using the
 532 staggered path-following scheme with $\Delta\Gamma = h$, $\frac{h}{2}$ and $\frac{h}{4}$. We observe that
 533 already with a step size of h , the correct fracture pattern is predicted. The ef-
 534 fect that the energy dissipation is increased is also observed here. As the step

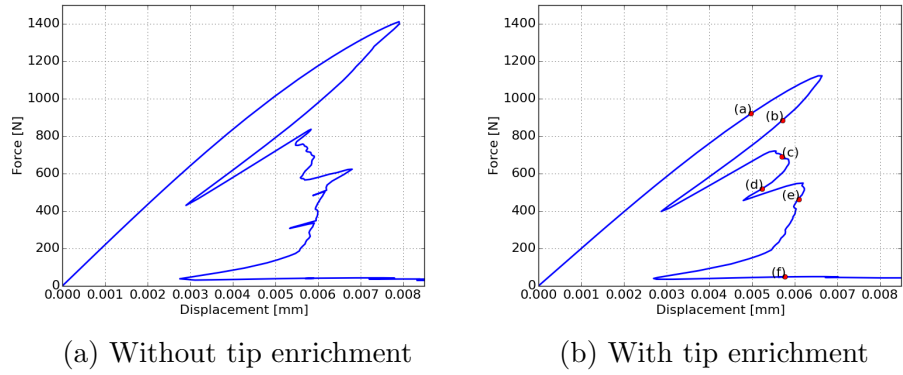


Figure 15: Comparison of the equilibrium path for the multiple pre-existing crack case computed using the fracture-controlled staggered scheme with and without tip enrichment.

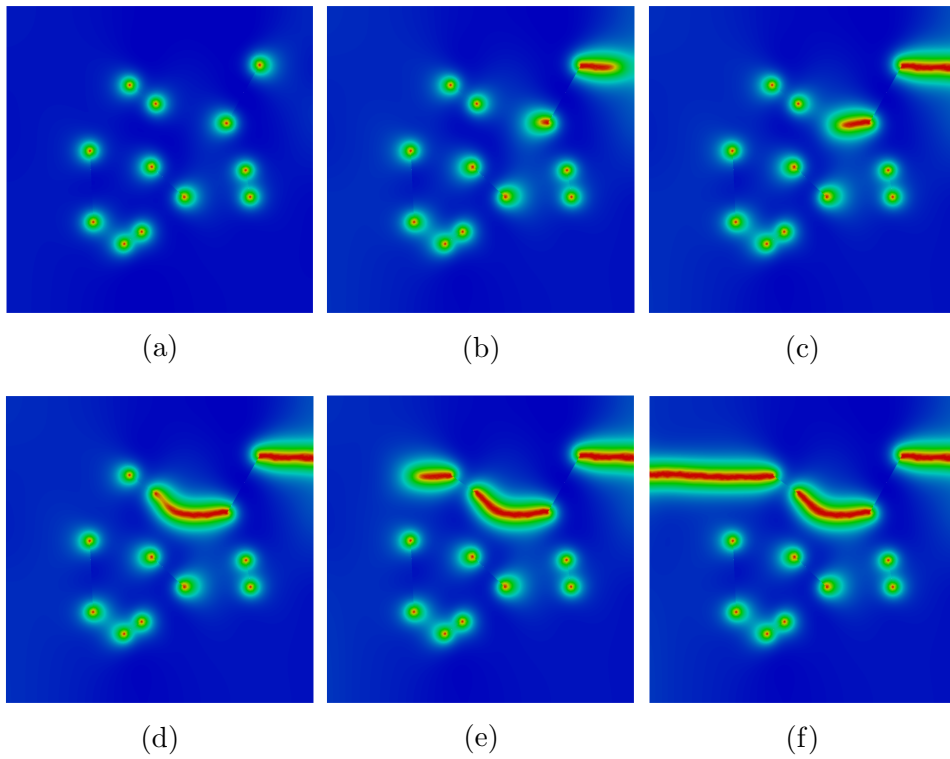


Figure 16: Six snapshots of the phase field for the tensile test with pre-existing cracks.

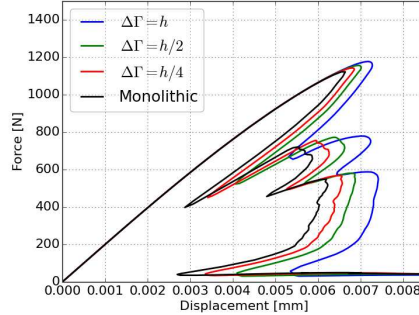


Figure 17: Force-displacement diagrams for the monolithic and staggered path-following schemes for the specimen with multiple pre-existing cracks.

535 size decreases, the force-displacement curve converges toward the Newton-
 536 Raphson case. It is important to note here that since the fractures evolve
 537 in stages, during the fracture process there is always one dominant fracture.
 538 This allows for the interpretation that the crack extends by approximately a
 539 single element in the case that $\Delta\Gamma = h$ is used. In the case that the evolution
 540 of a secondary crack is non-negligible, effectively a smaller crack incrementa-
 541 tion length (per crack) is used. In this sense, the choice of the crack length
 542 increment is a conservative choice, which permits its usage also in the case
 543 of complex fracture evolutions as considered here.

544 In Table 4 the monolithic scheme and staggered schemes with various
 545 fracture surface increments are compared in terms of the predicted fracture
 546 strength and total crack length. For all simulations regularized pre-existing
 547 crack tips are considered. We observe errors of a few percent for the staggered
 548 scheme with a step size of $h/4$, which is in agreement with the observations of
 549 the benchmark simulations discussed above. In terms of the number of sys-
 550 tem solves, this staggered simulation requires approximately half the number of
 551 solves of the monolithic scheme.

552 6. Conclusions

553 In this contribution we studied the application of a fracture-based path-
 554 following constraint for the simulation of phase-field cracks. The employed
 555 constraint is closely related to the dissipation-based constraint proposed in
 556 [16], but is formulated in terms of the phase field instead of stresses and
 557 strains (and rates thereof). Formulation of this constraint in terms of the

Scheme	$\Delta\Gamma$ ($\times h$)	n_{steps}	n_{iter}	n_{solve}	F_{peak} [N]	Γ_{ult} [mm]
Monolithic	0.62 (0.81)	195	3.10 (1.29)	605	1122	1.532
Staggered	1	209	1	209	1178	1.656
Staggered	$\frac{1}{2}$	327	1	327	1156	1.594
Staggered	$\frac{1}{4}$	540	1	540	1143	1.563

Table 4: Comparison of the monolithic and staggered path-following schemes for the specimen with multiple pre-existing cracks. For the monolithic scheme the mean value and standard deviation (in brackets) are given when applicable.

558 phase field invokes a natural decomposition of the phase-field problem and
559 the elasticity problem. Based on this decomposition, we developed a fracture-
560 controlled staggered solution procedure. The derivation of this staggered pro-
561 cedure proceeds in essentially the same manner as the derivation of the com-
562 monly used displacement-based staggered scheme [2] from a displacement-
563 controlled monolithic solution procedure.

564 There are two advantages to the use of a fracture-controlled path-following
565 constraint. First, this constraint permits for the simulation of snap-back phe-
566 nomena. In the studied numerical examples we have observed that snap-back
567 is typically encountered when a phase-field crack nucleates from a sharp crack
568 tip. By enriching the tips of pre-existing fractures with a phase field, this
569 snap-back behavior vanishes. The fracture-controlled constraint opens the
570 doors to a systematic study of this snap-back behavior, but this study is
571 considered beyond the scope of this manuscript. The second advantage of
572 fracture-control is that it provides a natural way to select the step size incre-
573 ments, this in contrast to the displacement-controlled staggered procedure.
574 By requiring that the cracks propagate gradually through the mesh, the step
575 size can be related to the characteristic element size. We have demonstrated
576 that also in the case of multiple cracks this way of selecting the fracture step
577 sizes renders meaningful results.

578 We have studied the performance of the fracture-controlled monolithic
579 and staggered solution procedures. Evidently, an advantage of the mono-
580 lithic scheme is that in every step the non-linear system to compute the so-
581 lution updates is solved exactly (up to the precision of the Newton-Raphson
582 process). In contrast, the fracture-based staggered scheme introduces an
583 additional source of errors by not resolving the non-linearities in every step.
584 The advantage of the staggered scheme is, however, that it is computationally
585 cheaper per load step by virtue of the fact that only a single decoupled elas-

586 ticity problem and phase-field problem is solved. In the studied numerical
587 examples we have found that the staggered scheme is capable of comput-
588 ing typical quantities of interest such as the peak load and total crack length
589 with errors of a few percent when step sizes of half the representative element
590 length scale are used. Overall it can be concluded that when a high accuracy
591 is required, the monolithic scheme is preferred. When minor inaccuracies
592 are acceptable, the staggered procedure can be expected to outperform the
593 monolithic scheme in terms of computational effort.

594 We note that herein we have considered a staggered solution procedure
595 with a single iteration per load step. It is possible to improve the accuracy of
596 this staggered procedure by using multiple sub-iterations per load step. This
597 will provide the opportunity to make a trade-off between computational effort
598 and solution accuracy. A detailed study of a staggered solution procedure
599 with sub-iterations is a topic of further study.

600 Acknowledgement

601 This work is part of the Industrial Partnership Programme (IPP) 'Com-
602 putational sciences for energy research' of the Foundation for Fundamental
603 Research on Matter (FOM), which is part of the Netherlands Organisation
604 for Scientific Research (NWO). This research programme is co-financed by
605 Shell Global Solutions International B.V. The research of C.V. Verhoosel was
606 funded by the NWO under the VENI scheme. All simulations in this work
607 were performed using the open source software package Nutils (www.nutils.org).

608 Appendix A. Internal force vectors and tangent stiffness matrices

For the phase-field fracture formulation introduced in Section 2 the inter-
nal and external force vectors follow directly from substitution of the finite
element basis function (5) as test functions in the weak form problem (4).
For the momentum equation, this yields:

$$f_{\text{int},I}^{\mathbf{u}} = \int_{\Omega} \boldsymbol{\sigma} : \nabla^s \mathbf{N}_I^{\mathbf{u}} dV \quad I = 1, \dots, n^{\mathbf{u}} \quad (\text{A.1a})$$

$$f_{\text{ext},I}^{\mathbf{u}} = \int_{\Gamma_N} \bar{\mathbf{t}} \cdot \mathbf{N}_I^{\mathbf{u}} dS \quad I = 1, \dots, n^{\mathbf{u}} \quad (\text{A.1b})$$

For the phase-field equation the following discrete equations are obtained:

$$f_{\text{int},I}^d = \int_{\Omega} \left[\left(\frac{\mathcal{G}_c}{l_c} + 2\mathcal{H} \right) d - 2\mathcal{H} \right] N_I^d + \mathcal{G}_c l_c \nabla d \cdot \nabla N_I^d dV \quad I = 1, \dots, n^d \quad (\text{A.2a})$$

$$f_{\text{ext},I}^d = 0 \quad I = 1, \dots, n^d \quad (\text{A.2b})$$

The corresponding tangent stiffness matrices follow by differentiation of these forces with respect to the nodal solution vectors as:

$$K_{IJ}^{uu} = \frac{f_{\text{int},I}^u}{\partial a_J^u} = \int_{\Omega} \nabla^s \mathbf{N}_I^u : \mathbb{C} : \nabla^s \mathbf{N}_J^u dV \quad (\text{A.3a})$$

$$K_{IJ}^{ud} = \frac{f_{\text{int},I}^u}{\partial a_J^d} = \int_{\Omega} 2(d-1) N_J^d (\nabla^s \mathbf{N}_I^u : \boldsymbol{\sigma}_0^+) dV \quad (\text{A.3b})$$

$$K_{IJ}^{du} = \frac{\partial f_{\text{int},I}^d}{\partial a_J^u} = \int_{\Omega} 2(d-1) N_I^d \left(\nabla^s \mathbf{N}_J^u : \frac{\partial \mathcal{H}}{\partial \boldsymbol{\varepsilon}} \right) dV \quad (\text{A.3c})$$

$$K_{IJ}^{dd} = \frac{\partial f_{\text{int},I}^d}{\partial a_J^d} = \int_{\Omega} \left(\frac{\mathcal{G}_c}{l_c} + 2\mathcal{H} \right) N_I^d N_J^d + \mathcal{G}_c l_c \nabla N_I^d \cdot \nabla N_J^d dV \quad (\text{A.3d})$$

609 where $\mathbb{C} = \partial \boldsymbol{\sigma} / \partial \boldsymbol{\varepsilon}$ is the material tangent, and $\boldsymbol{\sigma}_0^+$ is the tensile part of
 610 the virgin Cauchy stress tensor. Note that the tangent stiffness matrix is
 611 generally not symmetric, since

$$\frac{\partial \mathcal{H}}{\partial \boldsymbol{\varepsilon}} = \begin{cases} \boldsymbol{\sigma}_0^+ & \dot{\mathcal{H}} \geq 0 \\ 0 & \dot{\mathcal{H}} < 0 \end{cases}. \quad (\text{A.4})$$

612 **Appendix B. Equivalence of fracture control with energy release-** 613 **rate control**

614 Since in Griffith's theory for fracture the rate of dissipation is defined
 615 as the fracture toughness (\mathcal{G}_c) times the rate at which new fracture surface
 616 is created, the constraint equation derived in Section 3 relies on the same
 617 assumptions as the energy release rate path-following control in [16, 17]. In
 618 this appendix the relation between the path-following constraint developed
 619 in this work and the constraint of [16, 17] is examined.

620 Assuming infinitely small path-parameter increments, $\Delta\tau \rightarrow 0$, the con-
 621 straint equation (9) can be used to obtain

$$\dot{\Gamma}_{l_c}(d, \dot{d}) = \frac{1}{l_c} \int_{\Omega} d\dot{d} + l_c^2 \nabla d \cdot \nabla \dot{d} dV, \quad (\text{B.1})$$

622 which corresponds to the time derivative of the fracture surface area (8).
 623 Using the weak form (4) in combination with the Kuhn-Tucker conditions
 624 (3), this expression can be rewritten as

$$\dot{\Gamma}_{l_c} = \frac{2}{\mathcal{G}_c} \int_{\Omega} (1-d)\mathcal{H}\dot{d} dV = \frac{2}{\mathcal{G}_c} \int_{\Omega} (1-d)\psi_0^+ \dot{d} dV = -\frac{1}{\mathcal{G}_c} \int_{\Omega} \dot{g}\psi_0^+ dV, \quad (\text{B.2})$$

625 with degradation function $g(d) = (1-d)^2$. The rate of dissipation, defined
 626 as the external power minus the rate of elastic energy, can be written as:

$$\begin{aligned} \dot{D} = P - \dot{W} &= \int_{\Gamma_N} \bar{\mathbf{t}} \cdot \dot{\mathbf{u}} dS - \frac{d}{dt} \left[\frac{1}{2} \int_{\Omega} \boldsymbol{\sigma} : \boldsymbol{\varepsilon} dV \right] = \frac{1}{2} \int_{\Omega} [\boldsymbol{\sigma} : \dot{\boldsymbol{\varepsilon}} - \dot{\boldsymbol{\sigma}} : \boldsymbol{\varepsilon}] dV \\ &= \frac{1}{2} \int_{\Omega} \{ [\mathbb{C} : \boldsymbol{\varepsilon}] : \dot{\boldsymbol{\varepsilon}} - [\dot{g}\mathbb{C}_0^+ : \boldsymbol{\varepsilon} + \mathbb{C} : \dot{\boldsymbol{\varepsilon}}] : \boldsymbol{\varepsilon} \} dV = -\frac{1}{2} \int_{\Omega} \dot{g}\boldsymbol{\sigma}_0^+ : \boldsymbol{\varepsilon} dV = -\int_{\Omega} \dot{g}\psi_0^+ dV. \end{aligned} \quad (\text{B.3})$$

627 Combining with equation (B.2) shows that indeed $\dot{D} = \mathcal{G}_c \dot{\Gamma}_{l_c}$.

628 Appendix C. Phase-field tip enrichment

629 When simulating the fracture process in specimens with pre-existing cracks,
 630 in principle the tip-stresses will be singular when these cracks are modeled as
 631 strong discontinuities. Evidently, in a finite element context, finite stresses
 632 are obtained due to the regularizing effect of the interpolation functions.
 633 However, in principle, this regularizing effect is merely a discretization error.
 634 In relation to phase-field modeling, the tip stress does influence the value of
 635 the phase field at the tip [4], which causes a significant grid size dependence
 636 of the phase-field nucleation at the tip. In order to moderate this mesh de-
 637 pendence, in this work we enrich the fracture tips of pre-existing cracks with
 638 a phase field, thereby regularizing the stress field at these tips.

In order to enrich the tips of pre-existing cracks, we compute the history
 field prior to loading, $\mathcal{H}^0 : \Omega \rightarrow \mathbb{R}$. In order to obtain this field, we first solve
 the weak form problem for the phase field $d^0 : \Omega \rightarrow \mathbb{R}$:

$$\begin{cases} \text{Find } d^0 \in \mathcal{V}_{\text{tip}}^d \text{ such that:} \\ \int_{\Omega} d^0 e + l_c^2 \nabla d^0 \cdot \nabla e dV = 0 \quad \forall e \in \mathcal{V}_{\text{tip},0}^d \end{cases} \quad (\text{C.1})$$

with $\mathcal{V}_{\text{tip}}^d = \{d^0 \in H^1(\Omega) | d^0 = 1 \text{ on } \Gamma_{\text{tip}}\}$, with $\Gamma_{\text{tip}} \subset \Omega$ the set of crack tip points. Subsequently, we determine the corresponding history field, $\mathcal{H}^0 : \Omega \rightarrow \mathbb{R}$:

$$\begin{cases} \text{Find } \mathcal{H}^0 \in H^1(\Omega) \text{ such that:} \\ \int_{\Omega} 2l_c(1-d)\mathcal{H}^0 \mathcal{J} dV = \int_{\Omega} \mathcal{G}_c (d^0 \mathcal{J} + l_c^2 \nabla d^0 \cdot \nabla \mathcal{J}) dV \quad \forall \mathcal{J} \in H^1(\Omega) \end{cases} \quad (\text{C.2})$$

639 For the discretization of both weak form problems we employ linear finite
640 element spaces.

641 We note that an alternative approach to this tip-enrichment strategy is
642 to model the pre-existing fractures completely by phase-field fractures. An
643 advantage of this approach is that there is no need to create sharp discontinu-
644 ities in the mesh. However, the creation of such cracks is generally non-trivial
645 when they do not align with the finite element grid.

646 Bibliography

- 647 [1] B. Bourdin, G. A. Francfort, J. Marigo, The variational approach to
648 fracture, *Journal of Elasticity* 91 (2008) 5–148.
- 649 [2] C. Miehe, M. Hofacker, F. Welschinger, A phase field model for rate-
650 independent crack propagation: Robust algorithmic implementation
651 based on operator splits, *Computer Methods in Applied Mechanics and*
652 *Engineering* 199 (45–48) (2010) 2765 – 2778.
- 653 [3] B. Bourdin, C. J. Larsen, C. Richardson, A time-discrete model for
654 dynamic fracture based on crack regularization, *International Journal*
655 *of Fracture* 168 (2011) 133–143.
- 656 [4] M. J. Borden, C. V. Verhoosel, M. A. Scott, T. J. R. Hughes, C. M.
657 Landis, A phase-field description of dynamic brittle fracture, *Computer*
658 *Methods in Applied Mechanics and Engineering* 217–220 (2012) 77–95.
- 659 [5] C. Miehe, L. M. Schänzel, Phase field modeling of fracture in rubbery
660 polymers. part i: Finite elasticity coupled with brittle failure, *Journal*
661 *of the Mechanics and Physics of Solids* 65 (2013) 93–113.

- 662 [6] C. Miehe, F. Welschinger, M. Hofacker, A phase field model of elec-
663 tromechanical fracture, *Journal of the Mechanics and Physics of Solids*
664 58 (10) (2010) 1716 – 1740.
- 665 [7] C. V. Verhoosel, R. de Borst, A phase-field model for cohesive frac-
666 ture, *International Journal for Numerical Methods in Engineering* 96 (1)
667 (2013) 43–62.
- 668 [8] M. F. Wheeler, T. Wick, W. Wollner, An augmented-Lagrangian
669 method for the phase-field approach for pressurized fractures, *Computer*
670 *Methods in Applied Mechanics and Engineering* 271 (2014) 69–85.
- 671 [9] R. de Borst, M. A. Crisfield, J. J. C. Remmers, C. V. Verhoosel, *Non-*
672 *Linear Finite Element Analysis of Solids and Structures*, 2nd Edition,
673 Wiley, 2012.
- 674 [10] E. Riks, An incremental approach to the solution of snapping and buck-
675 ling problems, *International Journal of Solids and Structures* 15 (7)
676 (1979) 529–551.
- 677 [11] M. A. Crisfield, Accelerated solution techniques and concrete cracking,
678 *Computer Methods in Applied Mechanics and Engineering* 33 (1) (1982)
679 585–607.
- 680 [12] E. Ramm, *Strategies for tracing the nonlinear response near limit points*,
681 Springer, 1981.
- 682 [13] M. G. D. Geers, Enhanced solution control for physically and geomet-
683 rically non-linear problems. part I – the subplane control approach, *In-*
684 *ternational Journal for Numerical Methods in Engineering* 46 (2) (1999)
685 177–204.
- 686 [14] M. G. D. Geers, Enhanced solution control for physically and geomet-
687 rically non-linear problems. part II – comparative performance analy-
688 sis, *International Journal for Numerical Methods in Engineering* 46 (2)
689 (1999) 205–230.
- 690 [15] R. de Borst, Computation of post-bifurcation and post-failure behavior
691 of strain-softening solids, *Computers & Structures* 25 (2) (1987) 211–
692 224.

- 693 [16] M. A. Gutiérrez, Energy release control for numerical simulations of
694 failure in quasi-brittle solids, *Communications in Numerical Methods in*
695 *Engineering* 20 (1) (2004) 19–29.
- 696 [17] C. V. Verhoosel, J. J. C. Remmers, M. A. Gutiérrez, A dissipation-based
697 arc-length method for robust simulation of brittle and ductile failure, *International Journal for Numerical Methods in Engineering* 77 (9) (2009)
698 1290–1321.
699
- 700 [18] F. P. van der Meer, L. J. Sluys, A phantom node formulation with mixed
701 mode cohesive law for splitting in laminates, *International Journal of*
702 *Fracture* 158 (2) (2009) 107–124.
- 703 [19] J. Vignollet, S. May, R. de Borst, C. V. Verhoosel, Phase-field models
704 for brittle and cohesive fracture, *Meccanica* 49 (11) (2014) 2587–2601.